SABER: Symbolic Regression-Based Angle of Arrival and Beam Pattern Estimator

Shih-Kai Chou, *Member, IEEE*, Mengran Zhao, *Member, IEEE*, Cheng-Nan Hu, *Senior Member, IEEE*, Kuang-Chung Chou, *Member, IEEE*, Carolina Fortuna, and Jernej Hribar, *Member, IEEE*

***Abstract*—Accurate angle-of-arrival (AoA) estimation is essential for next-generation wireless communication systems to enable reliable beamforming, high-precision localization, and integrated sensing. Unfortunately, classical high-resolution techniques require multielement arrays and extensive snapshot collection, while generic machine-learning (ML) approaches often yield black-box models that lack physical interpretability. To address these limitations, we propose a symbolic regression (SR)-based ML framework. Namely, symbolic regression-based angle of arrival and beam pattern estimator (SABER), a constrained SR framework that automatically discovers closed-form beam pattern and AoA models from path loss measurements with interpretability. SABER achieves high accuracy while bridging the gap between opaque ML methods and interpretable physics-driven estimators. First, we validate our approach in a controlled free-space anechoic chamber, showing that both direct inversion of the known $\cos^n$ beam and a low-order polynomial surrogate achieve sub-0.5° mean absolute error (MAE). A purely unconstrained SR method can further reduce the error of the predicted angles, but produces complex formulas that lack physical insight. Then, we implement the same SR-learned inversions in a real-world, reconfigurable intelligent surface (RIS)-aided indoor testbed. SABER and unconstrained SR models accurately recover the true AoA with near-zero error. Finally, we benchmark SABER against the Cramér–Rao lower bounds (CRLBs). Our results demonstrate that SABER is an interpretable and accurate alternative to state-of-the-art and black-box ML-based methods for AoA estimation.**

***Index Terms*—Angle-of-arrival (AoA) estimation, reconfigurable intelligent surface (RIS), symbolic regression (SR).**

I. Introduction

As THE transition from 5G to 6G accelerates, the foundational pillars of 5G, which include Enhanced mobile broadband (eMBB), Ultra reliable low latency communications (URLLC)s, and Massive machine type communications (mMTC)s, will be significantly expanded and enhanced to support an even broader range of services and applications [1]. In particular, eMBB will offer higher capacity and coverage; URLLCs will evolve into Immersive, hyper reliable, and low-latency communication (IHRLLC), providing deterministic, resilient connectivity for time-critical domains such as self-driving vehicles and autonomous systems [2], and mMTCs will scale to connect vast numbers of devices in smart cities, digital twins, and pervasive sensing environments [3].

To realize the expanded capabilities of eMBB, IHRLLC, and mMTCs in 6G, directional communication is required. However, as 6G introduces new physical layer technologies that offer fine-grained control over spatial resources and operate at higher frequencies with tighter beamforming [4], alongside advanced techniques such as ultra (cell-free) massive Multiple-input–multiple-output (MIMO) [5], [6], and Reconfigurable intelligent surface (RIS) [7]. Consequently, precise beam alignment and low-latency Angle-of-arrival (AoA) estimation become first-order requirements for robust links, tracking, handover, and spatial reuse.

Current AoA estimators either depend on multiantenna arrays and numerous snapshots [8], which make them sensitive to calibration and Signal-to-noise ratio (SNR) while being computationally expensive [9]. Alternatively, they rely on data-hungry and black-box Machine learning (ML) models with limited interpretability and cross-scenario generalization [10]. Collectively, array/snapshot dependencies and black-box ML models hinder reliable and interpretable AoA estimation for timely beam alignment, tracking, and handover across deployment conditions.

These observations suggest that remaining gaps require methods that integrate measurement design with the estimation model, reduce reliance on extensive training data, and preserve a transparent connection to the underlying propagation physics. Addressing these needs calls for an approach that links the structure of the collected measurements with a method capable of capturing physical relationships in a data-efficient and interpretable manner. To overcome these limitations, we propose a physics-guided Symbolic regression (SR) framework that inverts beam patterns directly from the measured path loss coefficient, and further enables interpretable, ML-based AoA estimation. Specifically, we introduce the symbolic regression-based angle of arrival and beam pattern estimator (SABER). Moreover, SABER operates directly on a single scalar feature: the measured path loss coefficient, which allows us to recover closed-form, physically interpretable beam pattern expressions and AoA estimations.

Received 30 October 2025; revised 18 March 2026; accepted 7 April 2026. Date of publication 27 April 2026; date of current version 7 May 2026. This work was supported in part by European Commission NANCY Project under Grant 101096456; and in part by Slovenian Research Agency under Grant P2-0016, Grant J2-50071, and Grant MN-0009. The Associate Editor coordinating the review process was Dr. Emanuele Piuzzi. *(Corresponding author: Shih-Kai Chou.)*

Shih-Kai Chou, Carolina Fortuna, and Jernej Hribar are with the Jožef Stefan Institute, 1000 Ljubljana, Slovenia (e-mail: shih-kai.chou@ijs.si; carolina.fortuna@ijs.si; jernej.hribar@ijs.si).

Mengran Zhao is with the Centre for Wireless Innovation, Queen's University Belfast, BT3 9DT Belfast, U.K., and also with the School of Information and Communication Engineering, Xi'an Jiaotong University, Xi'an 710049, China (e-mail: mengran.zhao@qub.ac.uk).

Cheng-Nan Hu and Kuang-Chung Chou are with Asia Eastern University of Science and Technology, New Taipei City 220303, Taiwan (e-mail: fo011@mail.aeust.edu.tw; kcchou24g@gmail.com).

Digital Object Identifier 10.1109/TIM.2026.3687328

Unlike conventional regression methods that assume a predefined equation, SR is a type of ML that analyzes data to discover the underlying, human-readable mathematical formula that best fits the data, balancing accuracy with simplicity. By leveraging SABER, we can efficiently approximate beam patterns and AoA estimations, capturing crucial directional characteristics and simplifying computational demands in an interpretable way. Thus, SABER streamlines the estimation process, as well as provides interpretable, symbolic models suitable for real-time and resource-constrained applications inherent in the next-generation communication systems. We focus on AoA estimation with a single antenna at the receiver; transmitter-side beamforming and RIS are part of the link. Moreover, the receiver provides only a scalar S-parameter per frequency.

The primary contribution of this work is methodological: we introduce a physics-guided SR framework that learns interpretable, closed-form beam pattern and AoA estimators from scalar path loss measurements. More specifically, the contributions are as follows.

1) We propose SABER, a constrained SR-framework that discovers closed-form and physically interpretable mappings from the measured path loss coefficient to the beam pattern and AoA. By embedding lightweight antenna-physics priors into the SR search, SABER yields mathematical expressions that can be inspected and reused analytically, while balancing accuracy and interpretability.
2) We design a two-stage data collection and benchmarking protocol consisting of anechoic-chamber sweeps (Stage I, baseline verification) and indoor RIS-aided measurements (Stage II, system robustness validation), providing a reproducible template for evaluating SR-based estimators under both controlled and practical mmWave/RIS propagation conditions.
3) We demonstrate that SABER achieves sub-0.5° Mean absolute error (MAE) in AoA estimation and closely tracks the Cramér–Rao lower bound (CRLB) (within 10^{-3} degrees in the 50°–60° range), while an unconstrained SR baseline achieves marginally lower error (0.396° versus 0.42°) at the cost of physical interpretability.

The article is organized as follows. Section II reviews related work. Section III introduces the mathematical framework for path loss-based AoA estimation. Section IV details the proposed SR-based framework, SABER, and its workflow. Section V describes the two experimental setups: a controlled free-space measurement and a RIS-aided indoor testbed, along with the data collection procedures, while Section VI covers the model training parameters. Section VII presents the results, evaluating the SR-based methods and comparing their performance to the theoretical CRLB. Finally, Section VIII concludes the article and outlines future research directions.

II. Related Work

In this section, we first summarize the literature related to classical AoA estimation techniques, followed by Artificial intelligence (AI)/ML approaches.

A. Classical AoA Estimating Techniques

Traditionally, classical signal processing techniques such as Multiple signal classification (MUSIC) [11] and Estimation of signal parameters via rotational invariance techniques (ESPRITs) [12] are used for AoA estimation, and have been widely utilized due to their high resolution. These subspace-based algorithms decompose the covariance matrix of the received signals to identify the signal directions and offer precise AoA estimates. However, they often require a large number of snapshots acquired from a uniform antenna array and incur high computational complexity [13], making real-time deployment difficult. In addition, beamforming techniques such as the Minimum variance distortionless response (MVDR) beamformer [14] aim to enhance signal reception from the desired directions while suppressing interference and noise, but they too reach their limits in dynamic and complex environments.

Recent measurement-driven studies have further highlighted these challenges [15], [16], [17], [18]. For example, in [17], an experimental 5G New radio (NR) AoA system implemented with Universal software radio peripheral (USRP) devices demonstrated that even small phase and amplitude mismatches across antenna elements can severely reduce the accuracy of subspace methods, requiring extensive calibration and compensation procedures. Similarly, Ultrawideband (UWB)-based localization platforms [18] that jointly estimate distance and AoA rely on deterministic time-of-flight and phase relationships, achieving centimeter-level accuracy only when antenna geometry and multipath are well controlled. These systems illustrate how classical AoA approaches remain sensitive to hardware variations, multipath, and calibration errors, even when theoretically optimal. They also show that the effectiveness of an AoA estimator is deeply influenced by how the underlying measurements are collected, not only by the algorithm used. This observation motivates approaches that explicitly integrate the measurement procedure with the estimation model, as done through the two-stage measurement in our work.

To address these challenges, ML-based techniques have been introduced to learn data-driven mappings for AoA estimation. Building upon this paradigm, our work extends such approaches toward interpretable, physics-consistent modeling.

B. ML-Based Techniques

AI/ML approaches address the limitations of conventional beamforming by learning complex patterns from the measurement data. For instance, in Millimeter-wave (mmwave) and sub-Terahertz (THz) scenarios, Domae et al. [19] proposed a ML-based approach using only phase-less measurements of the received power, demonstrating a significant reduction in beam alignment overhead compared to exhaustive searches and an improvement over compressive sensing techniques in multipath environments [20]. In addition, Zhang et al. [21] investigated Deep learning (DL)-based techniques to predict transmitting beamforming based solely on historical Channel state information (CSI) without requiring current channel information in a Multi-input–single-output (MISO) downlink system.

A Long-short-term memory (LSTM)-based channel prediction module was proposed to improve the performance of prediction. Furthermore, a comprehensive evaluation of ML-based spatial-domain beam prediction and time-domain beam prediction was carried out within a realistic 3rd generation partnership project (3GPP)-compliant simulator [22]. It showed significant benefits in system-level Key performance index (KPI), such as user throughput and measurement overhead. Moreover, Xue et al. [23] jointly optimize probing-beam selection and beam prediction with an integrated neural network. Unlike traditional methods that utilize predefined and spatially regular beam patterns aimed to minimize the overhead and latency in a mmWave MIMO downlink system. Their model consists of two jointly trained components: a sampling network that learns optimal sampling patterns through a differentiable approximation of the sampling function, and a beam prediction network. Inspired by the physics of antenna arrays, the prediction network uses Convolutional neural network (CNN) and self-attention to select the best beams from the measured reference signal received power (RSRP). This adaptive method significantly outperforms conventional Deep neural network (DNN) approaches that rely on static beam sampling configurations. Unlike the approach proposed in [23], our model bypasses differentiable sampling and CNN/attention predictors, using SR to derive closed-form, physics-consistent inversions from a path-loss coefficient. This yields an interpretable beam pattern estimation.

ML-based methods have also shown promise in AoA estimation, reducing the need for extensive snapshots and computational resources. In particular, Ge et al. [24] highlighted that traditional AoA estimation algorithms face several limitations, such as the need for prior knowledge of the number of signal sources, sensitivity to coherent signals, and performance degradation in noisy environments, while DL-based methods address these challenges by reformulating AoA estimation as a pattern recognition problem using neural networks to learn the mapping from signal data to arrival angles. Although these methods are attractive, the performance is significantly affected by the SNR, the number of snapshots, antennas, and the number of signal sources.

A hybrid approach was proposed in [25] that combines the traditional AoA estimation method, that is, MUSIC, with regression-based ML models, such as Gaussian process and regression tree, to improve AoA estimation. The framework first utilizes the MUSIC spatial spectrum as a feature extraction step, where the resulting spectrum data is then fed into a regression model. This hybrid MUSIC-ML framework can compensate for the multipath effects, as MUSIC alone would provide an inaccurate weighted average of all paths. In addition, using MUSIC-processed data, the models need fewer input nodes, thereby reducing the computing complexity rather than raw measurements as input. The performance degradation caused by low SNR and an unknown number of sources has been studied in [26] and [27]. More specifically, Papageorgiou et al. [26] introduced a deep CNN specifically designed for AoA estimation in extremely low SNR environments. This is achieved by a CNN with 2-D convolutional layers trained on multichannel data, which includes I/Q samples and phases. The results showed a more robust prediction at both low and high SNRs. More advanced ML architectures have also been explored. In [28], transformer-based AoA estimators for Bluetooth low energy (BLE) signals leverage self-attention to model long-range dependencies in I/Q sequences, improving performance under multipath but further increasing model complexity and opacity. However, while such ML models effectively learn statistical mappings from signal features to recover AoA, they remain black-box estimators, which offer limited interpretability and little insight into the underlying physical relationships between path loss, gain, and angle. In contrast, SABER leverages SR to recover these dependencies in closed-form, providing both physical transparency and comparable accuracy.

Several new technologies also leverage ML-based methods to achieve accurate AoA estimation [29], [30], [31], [32], [33]. For example, in RIS-aided systems, Azhdari and Farhang [30] proposed directly embedding the RIS functionality into a neural network-based architecture, and creating a learnable RIS layer, allowing a more efficient and robust control mechanism over classic maximum-likelihood approaches. DL frameworks have proven particularly effective at learning complex mappings from signal data to arrival angles, with CNN consistently outperforming classical spectral-based algorithms, especially in challenging low SNR environments and multipath scenarios. However, these black-box approaches, while highly effective, offer limited insight into the underlying physical relationships governing the estimation process, making it difficult to understand, validate, or generalize the learned models beyond their training conditions.

These limitations highlight the broader potential for ML approaches that can discover hidden patterns and relationships in complex signal processing problems while maintaining interpretability, motivating the exploration of methods that can provide both accuracy and physical insight, such as SR. Classical beam pattern and AoA estimation rely on explicit algorithms but suffer from high complexity, whereas ML methods trade interpretability for flexibility and typically require high-dimensional features or large supervised datasets whose collection is often costly and tightly coupled to the measurement setup. SABER bridges this divide by discovering closed-form, physics-consistent relations directly from data. By using only a scalar path loss coefficient, SABER offers a balance between analytical transparency and learning-based adaptability.

III. Analytical Model for Path Loss to Beam Pattern Mapping

In this section, we describe two scenarios to demonstrate the method for calculating the total path loss coefficient during measurement in an indoor environment. We first consider a scenario in which the transmission takes place in a free space with far-field setup, and then a scenario in which a connection is established via RIS with no direct link between the transmitter and the receiver, and they are in the radiative near-field (Fresnel region), where the total path loss is calculated as the sum of path loss between the transmitter and the receiver,

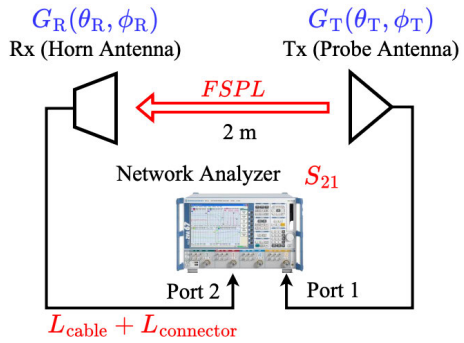

Fig. 1. System model of free-space scenario.

the antenna gains/beamforming, and the losses during the measurement. Consequently, the path loss coefficient can be defined as follows:

$$PL_{\_,\text{tot}} = PL_{\_} + \sum_{loss} L_{loss} - \sum_{gain} G_{gain} \tag{1}$$

where $PL_{\_}$ denotes the path loss between the transmitter and the receiver for the specific scenario, that is, FS for free space and RIS for RIS-aided scenario.

A. Free-Space Scenario

In this scenario, the transmitter (Tx) and receiver (Rx) are in their far-field regions. Therefore, the path loss coefficient is modeled using the Free-space path loss (FSPL) equation, denoted as PL_{FS}. It is defined as follows:

$$\begin{aligned} PL_{\text{FS}}\ [\text{dB}] &= 20\log_{10}(R) + 20\log_{10}(f) \\ &+ 20\log_{10}(4\pi) - 20\log_{10} c \end{aligned} \tag{2}$$

where R, f, and c are the distance between transmitter and receiver, the carrier frequency of the signal, and the speed of light, respectively. As depicted in Fig 1, during the measurement, the losses of the connector and the cable, denoted as $L_{\text{connector}}$ and L_{cable}, respectively, along with the gain of the transmitting and receiving antennas, G_T and G_R, are taken into account. As a result, the total path loss coefficient can be expressed as follows:

$$\begin{aligned} PL_{\text{FS,tot}}\ [\text{dB}] &= PL_{\text{FS}} + L_{\text{connector}} + L_{\text{cable}} \\ &- G_T(\theta_T, \phi_T) - G_R(\theta_R, \phi_R). \end{aligned} \tag{3}$$

Although the connectors and associated cables on both sides are calibrated using a short-open-load-through (SOLT) two-port calibration procedure on the R&S ZVA-40G vector network analyzer (VNA) prior to the RIS-aided system measurements, an additional 1 dB loss of male/female connectors transition in connection is included throughout the analysis to account for measurement uncertainty. Accordingly, the received power is computed based on the measured S_{21} (dB). Moreover, the terms $G_T(\theta_T, \phi_T)$ and $G_R(\theta_R, \phi_R)$ are defined as the gains of the transmitting and receiving antennas, respectively, as functions of the azimuth ($\theta_{\_}$) and elevation ($\phi_{\_}$) angles in the spherical coordinates.

For simplicity, we assume that both the transmitting and receiving antennas exhibit the same directional characteristics.

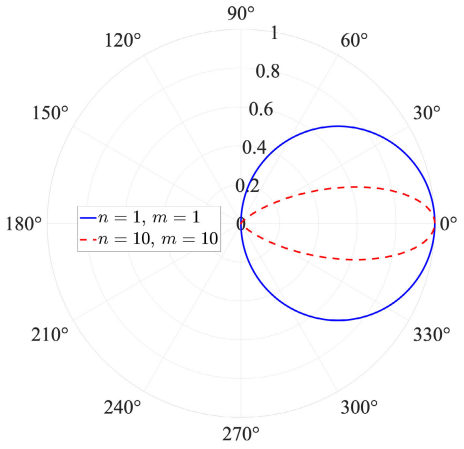

Fig. 2. Beam pattern with different n and m in polar coordinates.

Specifically, the gain of each antenna is modeled as the product of its maximum gain, $G_{\max}$, and its normalized radiation pattern, $U(\theta, \phi)$. Thus, the antenna gain $G(\theta, \phi)$ is given by the following equation:

$$G(\theta, \phi) = G_{\max} U(\theta, \phi). \tag{4}$$

Moreover, the normalized radiation pattern $U(\theta, \phi)$ can be modeled as follows:

$$\begin{aligned} &U(\theta, \phi) = \cos^n(\theta)\cos^m(\phi) \\ &\text{where}\quad \theta \in \left[0, \frac{\pi}{2}\right],\ \phi \in [-\pi, \pi] \end{aligned} \tag{5}$$

where n and m are the parameters determining the directivity of the antenna and the shape of the pattern [34]. In particular, as the values of n and m increase, the main lobe becomes narrower, resulting in a more focused and directional beam. This behavior is illustrated in Fig. 2, which shows the azimuth angle of the beam pattern for two sets of parameters. A small n and m produce a wider, less directional beam, whereas larger values have a narrower and higher directive beam. As a result, by substituting (3)–(5) in (1), the total FSPL can be rewritten as follows:

$$\begin{aligned} PL_{\text{FS,tot}}\ [\text{dB}] &= PL_{\text{FS}} + L_{\text{connector}} + L_{\text{cable}} \\ &- G_{T,\max} - G_{R,\max} \\ &- 10\left(n_T \log_{10}(\cos(\theta_T)) + m_T \log_{10}(\cos(\phi_T))\right. \\ &+ \left. n_R \log_{10}(\cos(\theta_R)) + m_R \log_{10}(\cos(\phi_R))\right). \end{aligned} \tag{6}$$

B. RIS-Aided Systems

The system model for a RIS-aided system is shown in Fig. 3. According to [35], the path loss coefficient, PL_{RIS}, for a RIS-aided system is typically modeled in the far-field. In our setup, where the aperture of the intelligent surface operates in the radiative near-field (Fresnel region), we adopt this standard power-scaling law as a baseline approximation for the angle-dependent loss, which is given as follows:

$$\begin{aligned} PL_{\text{RIS}} = \frac{G_T G_R}{(4\pi)^2}\left(\frac{ab}{R_{T,\text{RIS}} R_{\text{RIS},R}}\right)^2 \varepsilon_{\text{ap}}^2 \cos^2(\theta_{\text{axis}}) \\ , 0 \le \theta_{\text{axis}} \le \frac{\pi}{2} \end{aligned} \tag{7}$$

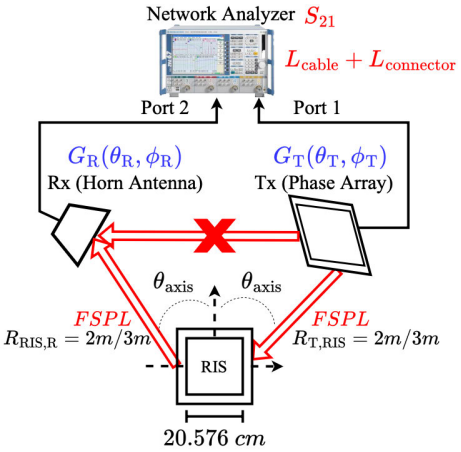

Fig. 3. System model of RIS-aided system.

where a, b, $R_{\text{T,RIS}}$, and $R_{\text{RIS,R}}$ are the length, the width of the RIS, the distances from the transmitter to the RIS and the RIS to the receiver, respectively. In addition, ε_{ap} is the aperture efficiency of the RIS and θ_{axis} is the angle between the incident wave and the optical axis of the RIS. This implies that the expression for the path loss from the source to the RIS is maximized when the transmitter is on the optical axis, that is, when $\theta_{\text{axis}} = 0$. Similar to the free-space scenario, we also consider the losses of the connector ($L_{\text{connector}}$), the transmission line (L_{cable}), and the power divider (L_{PD}). Particularly, the power divider has four layers, each layer introduces a 7.5 dB signal loss. In addition to the gain of the transmitter and receiver, there is a beamforming gain, G_{BF}, present due to the nature of the phase array. Therefore, by substituting (4) into (7), we can then rewrite (1) in decibels as follows:

$$\begin{aligned} PL_{\text{RIS,tot}}\,[\text{dB}] = {} & 10\left(\log_{10} G_{\text{T}}\left(\theta_{\text{T}}, \phi_{\text{T}}\right) + \log_{10} G_{\text{R}}\left(\theta_{\text{R}}, \phi_{\text{R}}\right)\right) \\ & + 20\left(\log_{10} a + \log_{10} b - \log_{10} R_{\text{T,RIS}}\right. \\ & - \left.\log_{10} R_{\text{RIS,R}} + \log_{10} \varepsilon_{\text{ap}} + \log_{10} \cos\theta_{\text{axis}}\right) \\ & + L_{\text{PD}} + L_{\text{connector}} + L_{\text{cable}} - G_{\text{BF}}. \end{aligned} \tag{8}$$

Building upon the analytical path loss models established in this section, we now introduce the proposed SR-based framework designed to empirically learn these relationships from measurement data.

IV. Proposed Constrained SR-Based ML Framework: SABER

We adopt SR to learn closed-form, interpretable relations between the measured path loss coefficient, beam pattern, and the AoA. SR has several major families. Evolutionary SR via Genetic programming (GP) refines expression trees through mutation, crossover, and selection; it remains a dominant approach because it can discover compact, human-readable formulas, though it can be compute-intensive in very large operator spaces [36]. Deep SR (DSR) uses an Recurrent neural network (RNN) policy trained with Reinforcement learning (RL) [37] [e.g., Risk-seeking policy gradient (RSPG), Priority queue training (PQT)] to generate expressions rewarded by fit, typically with normalized error-based rewards and search constraints to keep formulas meaningful. To overcome the downsides of pure GP or pure DSR, hybrid, neural-guided GP SR is proposed with neural proposals and priority queues to accelerate exploration [38]. Other lines include grammar/latent-variable SR (e.g., GrammarVAE) [39] and physics-inspired heuristics (AI Feynman) [40], which help with syntax or exploit symmetries but may struggle to recover exact formulas or do not perform a direct symbolic search.

Given our dataset size and the need for closed-form, physics-consistent inversions, we adopt GP-based SR for SABER. GP supports: 1) parsimony via complexity penalties and Pareto selection; 2) light domain priors that bias the search toward physically valid forms; and 3) constant-time inference once the expression is found, which are properties well aligned with timely AoA estimation. Moreover, Fig. 4 outlines the workflow and paper organization: we first describe how we conduct data collection in Section V (as shown in the first block of Fig. 4), followed by the proposed SABER framework in Section VI (highlighted in yellow), including training the SR-based method to reconstruct the beam patterns and estimate the AoA. Next, we validate the learned symbolic expressions and their predictive performances (marked in green). Finally, we benchmark against the CRLB to showcase how close they are to the theoretical lower bound on estimation error (marked in purple).

V. Data Collection for Model Training

In this section, we describe the measurement schemes used to train the proposed SR-based ML models, corresponding to the blue-highlighted block in Fig. 4. The experimental validation follows the two-stage scenario introduced in Section III, designed to rigorously bridge theoretical verification with practical application. Stage I (Fig. 1), conducted in an anechoic chamber, serves as a *baseline verification*. Its primary purpose is to validate the source model, specifically, when the transmitter beam pattern G_{Tx} is in an idealized environment, verifying that the SR structure accurately captures the fundamental physics behavior. Stage II (Fig. 3) applies the method to a RIS-aided indoor scenario to serve as a *system robustness validation*. This stage demonstrates the method's applicability in a practical environment. Finally, to rigorously assess statistical efficiency, the estimation accuracy in both scenarios is benchmarked against the fundamental theoretical bounds, specifically the CRLB.

A. Stage I: Anechoic Chamber Verification

We first quantify system behavior in a controlled environment to extract the beam pattern response. To accurately quantify the FSPL between two antennas, a Rohde and Schwarz ZVA40 VNA [41] is utilized. The experiments are carried out in a $7 \times 4 \times 3$ m^3 anechoic chamber under far-field conditions. The antennas are arranged at a fixed distance of 2 m, whereby the measurements are conducted across the frequency band from 26 to 31 GHz. In addition, the experimental configuration is depicted in Fig. 5, illustrating the spatial arrangement of the antennas within the anechoic chamber. The transmitting antenna is a probe antenna placed on the left side of the figure, while a rotatable platform is

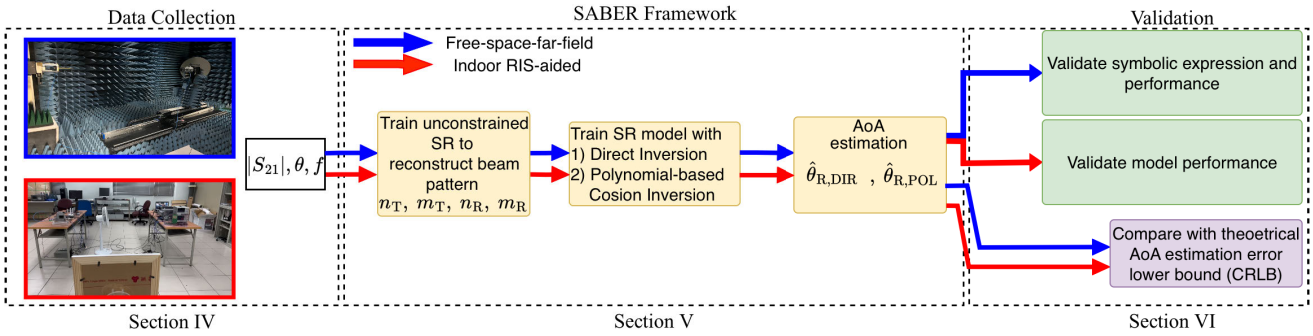

Fig. 4. Flowchart of the SABER framework: from data collection to verification.

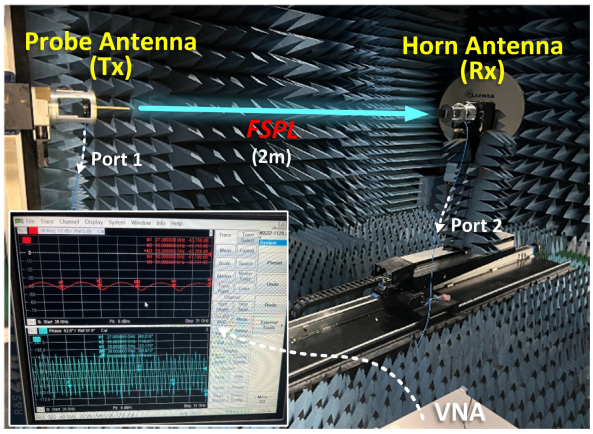

Fig. 5. Experiment setup for stage I (anechoic chamber verification). The probe antenna (Tx) is mounted on a motorized rotator at the left, and the horn antenna (Rx) is fixed at the right, forming a 2 m free-space path. Ports 1 and 2 of a Rohde and Schwarz ZVA40 VNA connect to the Tx and Rx, respectively, to measure the forward transmission coefficient $S_{21,FS}$ across 26–31 GHz. A representative sweep is shown in the lower left box.

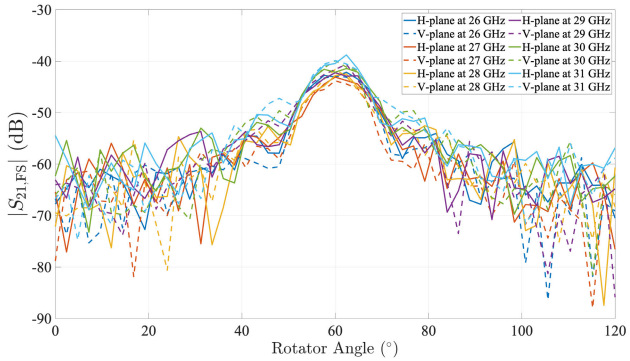

Fig. 6. Measurement with Rohde and Schwarz ZVA40 VNA for the forward transmission coefficient $S_{21,FS}$ across 26–31 GHz.

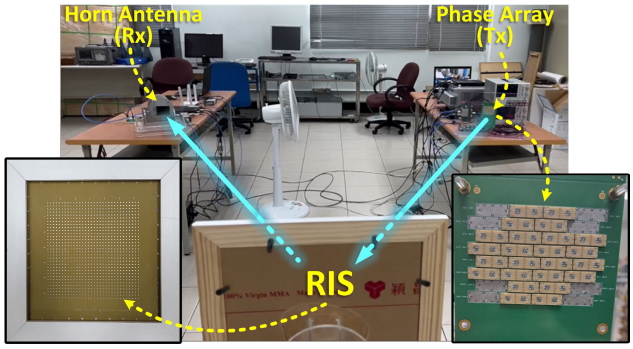

Fig. 7. Experimental setup for stage II (RIS-aided scenario). View from the RIS side: a 48-element phase array transmitter (right inset, phase array [42]) illuminates a passive 1024-element RIS (center) [43], which reflects toward a horn-antenna receiver located at the left side. The Tx-RIS and RIS-Rx links are LoS paths operating in the radiative near-field, as indicated by the cyan arrows.

placed on the right side of the figure, and the receiving antenna is a horn antenna. While this platform allows physical angular rotation from 0° to 120°, mapping a single scalar path loss coefficient to an angle can introduce ambiguity if the signal level drops below the highest secondary lobe of the receiving antenna. In our setup, however, utilizing a highly directional horn antenna can deeply suppress sidelobes and ensure that the measured path loss coefficients within this operational sweep range remain strictly on the main lobe, guaranteeing an unambiguous mapping. In particular, at a rotation angle of 60°, the antennas are directly facing each other, which optimizes signal reception and ensures maximum coupling efficiency. When working with symmetrical radiation patterns, both for the positive and negative θ_R angles, due to the symmetry of the pencil-beam radiation pattern, the effective AoA estimation range in both cases is 0°–60°. The probe (Tx) and horn antennas (Rx) have gains of 4.5 and 23.5 dBi, respectively.

Fig. 6 shows the measured S-parameter denoted as $S_{21,FS}$, expressed in dB, which characterizes the forward transmission coefficient of the system under test. Both horizontal (H-plane) and vertical (V-plane) polarization are measured. This parameter, critical for assessing signal attenuation, is recorded over a frequency range of 26–31 GHz in 1 GHz intervals, with measurements taken at incremental angular positions from 0° to 120° in 2.4° steps, in a total of 51 scanning points per frequency. The corresponding system model, illustrating the geometry and key parameters, is shown in Fig. 1. The data reveals that the maximum transmission, indicated by the peak $S_{21,FS}$ values, occurs around 60°–62.4° for both H- and V-planes, corresponding to the direct alignment of the antennas. The $S_{21,FS}$ values across the dataset range from approximately −88 to −39 dB, illustrating the variation in signal strength with respect to frequency and angular position.

B. Stage II: Real-World RIS-Aided Indoor System Verification

Building on the previous stage, the second stage is set in a realistic RIS-aided indoor testbed to verify that the

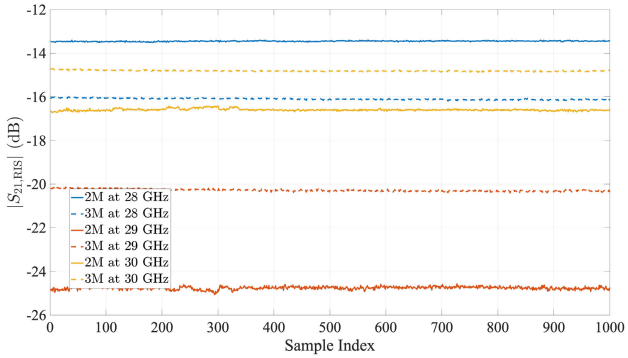

Fig. 8. Measurement for the forward transmission coefficient, $S_{21,\mathrm{RIS}}$ in stage II: RIS-aided indoor system. y-axis is the measured $|S_{21,\mathrm{RIS}}|$ value, while the x-axis indicates the sequential time snapshots of the S_{21} measurement.

measured S-parameter, $S_{21,\mathrm{RIS}}$, can be used to recover the AoA. The experiment setup is shown in Fig. 7. Specifically, the transmitter is equipped with a 48-element phase array [42], shown in the right inset, controlled by a beamformer (Renasas F6522 [44]), while the receiver is equipped with a horn antenna. In addition, a RIS with passive elements is set up to relay the signal from the transmitter to the receiver. The front side of the RIS is shown in the left inset of Fig. 7, the deployed RIS derived from the design in [43]; it has an area of 20.576 $\times$ 20.576 cm^2 and is implemented using truncated patch antennas printed on a 1-mm-thick FR-4 substrate. Furthermore, the total number of patch antennas is 1024. To achieve beam steering, we employ patch antennas with a shorted or opened load to simulate the ON/OFF status of a p-i-n diode, which is sequentially controlled column by column in the array. This configuration enables a progressive phase delay of 180° for beam steering in the azimuthal direction, denoted by θ_{axis}. In addition, the steering angle is determined by the element spacing d and the wavelength of the incident wave λ, which is given by the following equation:

$$\theta_{\mathrm{axis}} = \sin^{-1}\left(\frac{\lambda}{2d}\right). \tag{9}$$

In addition, the experiments are conducted at two different distances, and the detailed parameters are also shown in Fig 3. First, we set the distances between RIS to both the transmitter and the receiver as 2 m. Then, the distances are increased to 3 m, and we denote these two measurements as $S_{21,\mathrm{RIS},2\,\mathrm{m}}$ and $S_{21,\mathrm{RIS},3\,\mathrm{m}}$, respectively. Although the 2 and 3 m distances place the RIS aperture in the radiative near-field, we utilize the magnitude-based $|S_{21}|$ response, which exhibits a stable power envelope in this region, sufficient for the proposed ML-based estimation.

The temporal measurement of the forward transmission coefficient, $S_{21,\mathrm{RIS}}$, across 1000 snapshots is illustrated in Fig. 8, with a detailed statistical summary provided in Table I. It is visually apparent in the flat trend of the figure and quantitatively confirmed by the low standard deviations (all below 0.1 dB) in Table I, the channel exhibits high temporal stability within this time frame. For the sake of simplicity, we set the angle between both transmitter and receiver to 70°, that is, $\theta_{axis} = 35°$. Since the distance between the transmitter and the RIS, as well as between the RIS and the receiver, is known, we can obtain the AoA as 55° with simple geometric manipulations. Furthermore, due to the fact that the transmitter is equipped with a beamformer, there is an Nonline-of-sight (NLOS) connection between the transmitter and receiver, resulting in negligible signal strength.

TABLE I
MEAN AND STANDARD DEVIATION OF THE MEASURED FORWARD TRANSMISSION COEFFICIENT ($|S_{21,\mathrm{RIS}}|$) ACROSS 1000 SNAPSHOTS

Distance	Frequency	Mean $\lvert S_{21,\mathrm{RIS}}\rvert$ (dB)	Std. Dev. (dB)
2 m	28 GHz	-13.48	0.02
	29 GHz	-24.76	0.08
	30 GHz	-16.61	0.02
3 m	28 GHz	-16.08	0.02
	29 GHz	-20.26	0.03
	30 GHz	-14.81	0.02

The S-parameters are measured at the 28, 29, and 30 GHz frequencies. As detailed in Table I, the measurement results reveal that $S_{21,\mathrm{RIS},3\,\mathrm{m}}$ at 28 GHz has a mean transmission coefficient of −16.08 dB, which is approximately 2.6 dB lower than the mean value of −13.48 dB for $S_{21,\mathrm{RIS},2\,\mathrm{m}}$. However, this trend does not persist across the other frequencies, which emphasizes the dominant, frequency-selective role of the RIS. Notably, a significant signal degradation is observed at 29 GHz for the 2 m configuration, where the mean value of $S_{21,\mathrm{RIS},2\,\mathrm{m}}$ drops to −24.76 dB, far weaker than the −20.26 dB of $S_{21,\mathrm{RIS},3\,\mathrm{m}}$, indicating the formation of a deep, destructive interference null for this geometry. Conversely, at 30 GHz, the 3 m link is superior, with its mean $S_{21,\mathrm{RIS},3\,\mathrm{m}}$ of −14.81 dB outperforming the −16.61 dB of $S_{21,\mathrm{RIS},3\,\mathrm{m}}$.

VI. DEVELOPMENT OF SABER

As shown in Fig. 4, data collection is followed by model training and validation, which are, respectively, highlighted in red and green blocks. We train SR models with an open-source tool: PySR [45]. In addition, the unconstrained SR is considered as the baseline estimator, which learns a free-form mapping $g_{\mathrm{SR}}(\cdot)$. It can be expressed as follows:

$$\hat{\theta}_{\mathrm{R,SR}} = g_{\mathrm{SR}}\left(|S_{21,\_}|_{\mathrm{lin}}\right) \tag{10}$$

where $|S_{21}|_{\mathrm{lin}}$ denotes the measured S-parameter in linear scale. Moreover, expression trees are built using unary functions, including $\{\cos(\cdot), \sin(\cdot), \log_{10}, |\cdot|\}$, while the mathematical operations are limited to addition, subtraction, multiplication, and division. In addition, we set the number of evolutionary iterations to 5000 and the maximum depth to 10, and Pareto selection on error complexity. In particular, we define the differential path loss, ΔPL, which is calculated as follows:

$$\Delta PL = PL_{\_,\mathrm{tot}} - PL_{\_}. \tag{11}$$

The proposed framework first applies unconstrained SR to extract beam pattern parameters n_{T}, m_{T}, n_{R}, and m_{R}. Subsequently, two physics-guided estimation methods: direct inversion and polynomial-based cosine inversion are proposed for estimating AoA.

A. SABER: Direct Inversion

In this approach, we leverage the analytically known cosine-shaped antenna beam pattern to reverse the mapping from normalized path loss to AoA. Specifically, we fix the receive directivity (n_{R}) and fit only a single additive offset that is injected into the model to obtain the angle, denoted as $\hat{\theta}_{\mathrm{R,DIR}}$, and it is expressed as follows:

$$\hat{\theta}_{\mathrm{R,DIR}} = \arccos\left(10^{|S_{21,-}|}\right) + \text{offset}. \tag{12}$$

B. SABER: Polynomial-Based Cosine Inversion

Inspired by the fact that cosine function can be well approximated by low-order polynomials, in this approach, we direct fit a quadratic surrogate for $\cos(\hat{\theta}_{\mathrm{R}})$, that is, $\cos\theta \approx a(\Delta PL)^2 + b(\Delta PL) + c$, and then we can obtain the angle with $\arccos(\cdot)$. As a result, the estimated angle can then be expressed as follows:

$$\hat{\theta}_{\mathrm{R,POL}} = \arccos\left(10^{\frac{a(\Delta PL)^2 + b(\Delta PL) + c}{10n_{\mathrm{R}}}}\right). \tag{13}$$

The primary advantage of using this polynomial surrogate is computational efficiency. Unlike the direct inversion method, which requires evaluating an exponential function to invert the logarithmic path loss, the polynomial approach approximates the mapping using only fundamental arithmetic operations, such as multiplication and addition. This reduction in complexity makes it particularly suitable for deployment on resource-constrained edge devices or low-power controllers where computing transcendental functions is costly.

To consolidate the methodologies described in this section, we present our complete framework in Algorithm 1. The algorithm formalizes the key procedures for model training (Fit) and angle estimation (Predict).

Algorithm 1 Proposed SABER Framework

Require: measured path loss PL_{meas} (or $|S_{21}|$), training labels θ_{R}; mode $m \in \{\mathrm{DIRECTINV}, \mathrm{POLYCOSINV}\}$; PySR hyperparameters: n_{iter}=5000, maxsize=10; operator sets: $\{\cos, \sin, \exp, \log_{10}, |\cdot|, +, -, \times, \div\}$

Ensure: closed-form estimator $g_{\mathrm{SR}} : PL \mapsto \hat{\theta}_{\mathrm{R}}$

Initialization:

1: compute $\Delta PL \leftarrow PL_{\mathrm{meas}} - PL_{\mathrm{model}}$ ▷ Eq. 12
2: initialize radiation pattern $U(\theta, \phi)$
3: fit $(G_{\max}, \theta_{\mathrm{R}}, \theta_{\mathrm{T}})$ in $G(\theta, \phi) = G_{\max} U(\theta, \phi)$, find n/m_{R} and n/m_{T}
4: set $G_{\mathrm{dB}} \leftarrow 10\log_{10} G(\theta, \phi)$
5: **if** m = DIRECTINV **then** ▷SABER: Direct Inversion
6: define the estimator for x:

$$g_{\mathrm{SR}}(x) = \arccos\left(10^{\frac{x}{10n_{\mathrm{R}}}}\right) + \text{offset}$$

7: fit with PySR
8: **else if** m = POLYCOSINV **then** ▷SABER: Polynomial-based Cosine Inversion
9: define polynomial surrogate of cosine function $q(x)$
10: define the estimator for $q(x)$:

$$g_{\mathrm{SR}}(x) = \arccos(\min\{1, \max\{-1, q(x)\}\})$$

11: fit with PySR (Pareto selection: validation error vs. expression size)
12: **end if**
13: **return** g_{SR}
14: **function** PREDICT(PL_{test}, g_{SR})
15: $x \leftarrow PL_{\mathrm{test}}$
16: **return** $g_{\mathrm{SR}}(x)$
17: **end function**

First, it begins by taking the measured path loss coefficient as input PL_{meas} (or equivalently, the magnitude of the scattering parameter $|S_{21}|$) together with the ground-truth AoA labels θ_{R}. The algorithm can operate in one of two modes: direct inversion or polynomial-based cosine inversion. A set of hyperparameters for the SR engine (PySR) is also defined, including the number of iterations, maximum expression size, and the set of mathematical operators allowed during the symbolic search. The goal of the algorithm is to produce a closed-form estimator g_{SR} that maps path loss PL to the predicted AoA ($\hat{\theta}_{\mathrm{R}}$). This is described in the required and ensure part of the algorithm and followed by the initialization part of the algorithm (labeled as lines 1–4). SABER first computes the path loss difference $\Delta PL = PL_{\mathrm{meas}} - PL_{\mathrm{model}}$, which represents the deviation of the measured signal from the ideal theoretical model. It then initializes the radiation pattern of the antenna ($U(\theta, \phi)$) and fits the parameters that define its shape, namely $G_{\max}$, θ_{R}, and θ_{T}. More importantly, $G_{\max}$ is learned directly from the measurement data during this initialization step (Algorithm 1, Line 3). Therefore, any constant errors in the characterization of system losses, such as cable attenuation or connector losses, will be automatically absorbed into the learned pattern. This ensures that SABER remains robust and accurate even without precise prior knowledge of the total link budget. From this, it extracts n/m_{R} and n/m_{T} that characterize the beam directivity for both the receiver and transmitter. The antenna gain is then converted into decibel scale as $G_{\mathrm{dB}} = 10\log_{10} G(\theta, \phi)$, preparing the data for SABER. Conceptually, this step corresponds to the SABER framework in Fig. 4: first yellow block, where the reconstruction of the beam pattern parameters from measurement data happens.

Next, the algorithm proceeds according to the selected mode. If the direct inversion mode is chosen, SABER defines an estimator based on the analytical inversion of the cosine relationship between path loss and incident angle. Specifically, it uses $g_{\mathrm{SR}}(x) = \arccos(10^{x/(10n_R)}) + \text{offset}$. PySR is then used to fit this expression and refine the result through SR. If the polynomial-based cosine inversion mode is chosen instead, the algorithm defines a polynomial surrogate $q(x)$ to approximate the cosine term within its valid range of $[-1, 1]$. The estimator is then expressed as $g_{\mathrm{SR}}(x) = \arccos(\min\{1, \max\{-1, q(x)\}\})$, ensuring that physical constraints are respected. PySR fits this surrogate polynomial, balancing the tradeoff between model accuracy and expression complexity through Pareto optimization. This corresponds to the second yellow

block in the SABER framework in Fig. 4 and lines 5–13 in Algorithm 1.

After training in either mode, the algorithm returns the learned symbolic model g_{SR}, which serves as the closed-form mapping between path loss measurements and AoA (line 14–17 in Algorithm 1). In practice, this model is used for inference on unseen data, which the algorithm defines in the predict function. During prediction, a new path loss coefficient PL_{test} is passed to the trained estimator g_{SR}, which outputs the predicted AoA $\hat{\theta}_{\text{R}}$. This corresponds to the last yellow block "AoA Estimation" of SABER framework in Fig. 4, where the outputs $\hat{\theta}_{\text{R,DIR}}$ and $\hat{\theta}_{\text{R,POL}}$ are produced.

Finally, although not part of the algorithm itself, these estimated angles are validated experimentally. The symbolic expressions are first analyzed for interpretability and physical consistency, and then their estimation performance is compared against measured ground truth as well as the theoretical lower bound given by the CRLB. This matches the validation section of Fig. 4, where both the SR results and their numerical accuracy are evaluated.

The performance metrics in this work are MAE and Root-mean-square error (RMSE), which quantify, respectively, the average absolute error and the root-mean-square (rms) error. For N samples with ground-truth angles $\{\theta_i\}_{i=1}^{N}$ and estimates $\{\hat{\theta}_i\}_{i=1}^{N}$, these two performance metrics are defined as follows:

$$\text{MAE} = \frac{1}{N}\sum_{i=1}^{N}|\hat{\theta}_i - \theta_i| \tag{14}$$

and

$$\text{RMSE} = \sqrt{\frac{1}{N}\sum\nolimits_{i=1}^{N}\left(\hat{\theta}_i - \theta_i\right)^2}. \tag{15}$$

VII. Results and Discussions

In this section, we demonstrate the results of the unconstrained SR-based solutions and SABER for both beam pattern and AoA estimations in the aforementioned scenarios and measurements. Our focus is on the azimuth angle, θ, which is directly related to the values of n_{T} and n_{R}.

A. Stage I (Anechoic Chamber) Results

Automatically Learning to Estimate the Directivity Parameters: By applying the SR-based method, we can determine all directivity-related parameters, which include n_{T}, n_{R}, m_{T}, and m_{R}. Our findings from this method indicate that n_{T} and m_{T} are 1, while n_{R} and m_{R} are 28. As a result, the expression in (6), can be rewritten as follows:

$$\begin{aligned} PL_{\text{FS,SR}}\ [\text{dB}] = {} & FSPL - G_{\text{T,max}} - G_{\text{R,max}} \\ & - 10\left(\log_{10}\left(\cos\left(\theta_{\text{T}}\right)\right) + \log_{10}\left(\cos\left(\phi_{\text{T}}\right)\right)\right. \\ & \left. + 28\cdot\left(\log_{10}\left(\cos\left(\theta_{\text{R}}\right)\right) + \log_{10}\left(\cos\left(\phi_{\text{R}}\right)\right)\right)\right). \end{aligned} \tag{16}$$

We present the comparison between the measured beam pattern and the estimated one with the cosine function in Fig. 9, and the normalized cosine-pattern reproduces the measured half-power beamwidth to within a few degrees and aligns closely with the peak boresight amplitude once scaled to the same reference level. $\cos^{28}(\theta)$ is symmetric and free of sidelobes. However, it cannot capture the small amplitude ripples, asymmetries, and null depths observed in measurements. Thus, the approximation based on the cosine function offers an excellent first-order approximation of the main lobe. This is especially useful in theoretical analyses, where more detailed models or measured-data fits are required when sidelobe levels or pattern irregularities must be predicted with high fidelity.

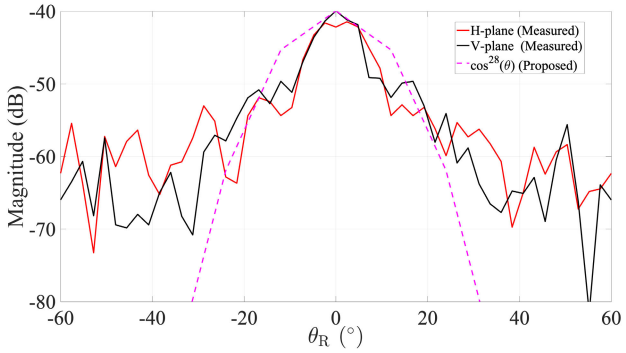

Fig. 9. Comparison of magnitude between probe antenna and the cosine-approximation in stage I: anechoic chamber verification.

Automatically Learning to Estimate the AoA: Once we have captured the theoretical approximation of the beam pattern, we can then utilize SR to search for the AoA with respect to the path loss coefficients. Furthermore, the three aforementioned SR-based AoA estimators are benchmarked, where the performance (in MAE) and the final expression are summarized in Table II. As we can observe from the results in column 2, Table II, although the unconstrained SR model (row 1) delivers the lowest MAE (0.396°), it does so by combining transcendental and arithmetic operations in a way that offers little physical insight into the underlying propagation or beam pattern. In contrast, SABER explicitly links to known beam patterns (row 2 and 3), with direct inversion having 14 times better accuracy than the polynomial-based method. Furthermore, there is a tradeoff between a minor loss in accuracy and achieving clear interpretability and consistency with theoretical beam pattern behavior. This tradeoff indicates that even a minimal amount of prior knowledge, such as the connection between the path loss coefficient and the beam pattern, when integrated with SR, results in models that are both highly accurate and easily interpretable according to column 2 and 3 in Table II. By enforcing the known pattern structure (or by approximating it with a low-order polynomial), we achieve high AoA accuracy while maintaining a direct mapping to the antenna design. In contrast, a purely unconstrained SR-matching can achieve slightly lower errors of the predicted angles, but at the expense of physical transparency and out-of-sample behavior guarantees.

B. Stage II (RIS-Aided Systems) Results

Automatically Learning to Estimate the Beam Pattern: We use the same method as in the Stage I to obtain the beam pattern for the transmitter and receiver, and we can arrive at 4 and 1, respectively. Moreover, in this setup, the transmitter

TABLE II

SUMMARY OF SR-BASED APPROACHES, INCLUDING THE FINAL INTERPRETABLE EXPRESSIONS AND THE PERFORMANCE IN MAE

Approach	MAE (°)	Final interpretable expression
Unconstrained SR	0.396	$\hat{\theta}_{\mathrm{R,SR}} = 0.53076 \sin\left(\sin(0.12336\, PL_{\mathrm{FS,tot}} + \theta_{\mathrm{T}})\right)$
SABER: Direct Inversion	0.42	$\hat{\theta}_{\mathrm{R,DIR}} = \arccos\left(10^{\Delta PL/(10\, n_{\mathrm{R}})}\right) + 0.05813$
SABER: Polynomial-based Cosine Inversion	5.96	$\hat{\theta}_{\mathrm{R,POL}} \approx \arccos(0.03879\, \Delta PL^2 + 0.1165\, \Delta PL + 0.8303)$

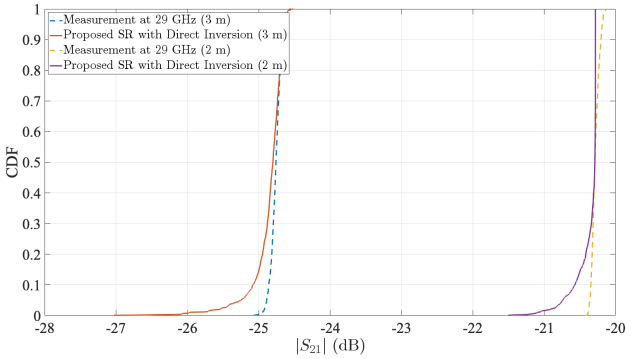

Fig. 10. CDF of the measured $|S_{21}|$ data in stage II and the analytical approximation in (17) via Monte Carlo simulation.

beamwidth is designed to fully illuminate the RIS aperture. While this ensures the utilization of all reflecting elements, it inevitably results in some spillover loss. However, rather than modeling the exact geometric efficiency ($\varepsilon_{\mathrm{ap}} < 1$), we adopt the ideal baseline ($\varepsilon_{\mathrm{ap}} \approx 1$) and rely on the SR framework to learn the effective system gains from the data. Consequently, any efficiency reduction due to spillover or element losses is automatically absorbed into the fit antenna gain parameters (G_{eff}) during the training process. Therefore, we can rewrite the path loss coefficient of the RIS-aided system in (8) as follows:

$$\begin{aligned} PL_{\mathrm{RIS,tot}}\ [\mathrm{dB}] = 10\,\big(&4\log_{10} G_{\mathrm{T,max}} \cos\left(\theta_{\mathrm{T}}, \phi_{\mathrm{T}}\right) \\ &+\ \log_{10} G_{\mathrm{R,max}} \cos\left(\theta_{\mathrm{R}}, \phi_{\mathrm{R}}\right)\big) \\ &+\ 20\,\big(\log_{10} a + \log_{10} b - \log_{10} R_{\mathrm{T,RIS}} \\ &-\ \log_{10} R_{\mathrm{RIS,R}} + \log_{10} \cos\theta_{\mathrm{axis}}\big) \\ &+\ L_{\mathrm{PD}} + L_{\mathrm{connector}} + L_{\mathrm{cable}} - G_{\mathrm{BF}}. \end{aligned} \tag{17}$$

We take the measurement at 29 GHz as an example to show that the analytical approach in (17) closely reproduces the measured $|S_{21}|$ distributions for both 2 and 3 m configurations in Fig. 10. The Cumulative distribution function (cdf) [46] slopes and spreads match well, with only a small systematic offset of less than 0.3 dB for both distances, indicating that the analytical angle-dependent model captures the dominant variability observed in practice. To generate the simulated distributions, a Monte Carlo procedure is applied in which the transmitter and receiver pointing offsets θ_{T} and θ_{R} are drawn from truncated Gaussian distributions centered at boresight with standard deviation $\sigma_{\mathrm{PL}} = 3°$. These angular offsets are then inserted into (8), and the process is repeated 3000 times to obtain a modeled path loss distribution for each distance.

Since we have already acquired the AoA from the setup in Section V, that is, $\theta_{\mathrm{R}} = 55°$. We can take it as ground truth and use an SR-based method for recovering the information of the angle. Building on the findings from the free-space analysis, the same estimation methodologies are applied to the more complex RIS-aided propagation environment. The results are shown in Table III.

TABLE III

AOA ESTIMATION MAE OF THREE SR-BASED INVERSION METHODS IN A RIS-AIDED INDOOR SETUP (IDENTICAL MAE AT 2 AND 3 M FOR BOTH TX-RIS AND RIS-RX LINK)

Approach	MAE (°)	Final expression ($\hat{\theta}_{\mathrm{R}}$ in radians)
Unconstrained SR	6.53×10^{-7}	0.9599
SABER: Direct Inversion	6.53×10^{-7}	0.9599
SABER: Polynomial-based Cosine Inversion	0.78	0.9736

Automatically Learning to Estimate the AoA: Stage II applies the same SR-based inversion methods in the RIS-aided indoor testbed at both 2 and 3 m. As shown in Table III, both the unconstrained SR and SABER with direct inversion approach (row 1 and 2) converge to the same closed-form cosine model and achieve a virtually zero MAE (6.53×10^{-7}) (column 2), effectively recovering the true 55° angle with negligible error (column 3). In contrast, the polynomial-based cosine inversion (row 3) fits a low-order surrogate to the cosine response, resulting in a larger error of 0.78°, which is consistent at both 2 and 3 m. This confirms that imposing the known beam pattern structure remains both interpretable and highly accurate even in the more complex, two-hop RIS propagation environment. Meanwhile, the unconstrained SR approach in this fixed-angle verification also yielded an interpretable model with near-zero error, suggesting that prior beam pattern knowledge is not strictly necessary when estimating a single, fixed AoA. By contrast, the AoA estimation with multiangle measurement, the same unconstrained SR produced highly complex expressions. These results indicate that while unconstrained SR achieves high accuracy in both stages, its ability to balance accuracy and interpretability emerges when estimating a single, deterministic angle.

C. Comparison to CRLB

CRLB is commonly used to benchmark the performance of an estimator, as it establishes the lower bound of Mean square error (mse) of any unbiased estimator [47], [48]. This is shown as the last block in Fig. 4 (highlighted in yellow). Note that standard array-based estimators (e.g., MUSIC, ESPRITs) are excluded from this comparison because they require multielement phase data, which is unavailable in our single-antenna scalar magnitude setup. For the single-link signal model of Section III, we can then express the received signal as follows:

$$\mathbf{y} = \alpha h(\theta)\, \mathbf{x} + \mathbf{n} \tag{18}$$

where upper and lower case letters denote matrices and vectors, respectively. θ denotes the AoA, and $\alpha \in \mathbb{C}$ is an angle-independent complex gain capturing all residual amplitude and phase factors not included in $h(\theta)$. More specifically, when a calibration tone at the peak gain direction θ_{pk} is available, the magnitude of the unknown gain, $|\alpha|$, is fixed by the following equation:

$$|\alpha| = \frac{\left|S_{21}\left(\theta_{\text{pk}}\right)\right|_{\text{lin}}}{h\left(\theta_{\text{pk}}\right)}. \tag{19}$$

We assume the phase of α is modeled as uniformly distributed over $[0, 2\pi)$. On the other hand, $h(\theta)$ is the deterministic, angle-dependent gain obtained from the path loss expressions in (3) and (8). Furthermore, $\mathbf{x}$ is the known data stream, with $\|\mathbf{x}\|^2 = 1$. In the absence of a dedicated calibration, we assume the receiver noise ($\mathbf{n}$) follows a zero-mean circularly symmetric complex Gaussian distribution, that is, $\mathbf{n} \sim \mathcal{CN}(0, \sigma^2 \mathbf{I}_M)$. Since $|\alpha|$ is known, the vector of unknown real-valued parameters is

$$\boldsymbol{\eta} = \left[\theta, \phi_\alpha, \sigma^2\right]^T. \tag{20}$$

The mean received signal is $\mathbb{E}\{\mathrm{y}\} = \boldsymbol{\mu}(\theta, \phi_\alpha) = |\alpha| e^{j\phi_\alpha} h(\theta)\mathbf{x}$. Its derivatives with respect to the unknown parameters are

$$\frac{\partial \boldsymbol{\mu}}{\partial \theta} = |\alpha| e^{j\phi_\alpha} h'(\theta)\,\mathbf{x} \tag{21}$$

$$\frac{\partial \boldsymbol{\mu}}{\partial \phi_\alpha} = j|\alpha| e^{j\phi_\alpha} h(\theta)\,\mathbf{x} \tag{22}$$

where $h'(\theta) = \partial h(\theta)/\partial\theta$. As a result, the complex-Gaussian log-likelihood yields the Fisher information matrix

$$\mathbf{I}(\theta, \phi_\alpha) = \frac{2M|\alpha|^2}{\sigma^2} \times \begin{bmatrix} |h'(\theta)|^2 & -\operatorname{Im}\{h'(\theta)^* h(\theta)\} \\ -\operatorname{Im}\{h'(\theta)^* h(\theta)\} & |h(\theta)|^2 \end{bmatrix} \tag{23}$$

where $\operatorname{Im}\{\cdot\}$ represent taking the imaginary part of the variable. By inverting $\mathbf{I}(\theta, \phi_\alpha)$ yields the general CRLB for θ

$$\operatorname{Var}\left\{\hat{\theta}\right\} \geq \frac{\sigma^2}{2M|\alpha|^2} \frac{|h(\theta)|^2}{|h(\theta)|^2 |h'(\theta)|^2 - \left(\operatorname{Im}\{h'(\theta)^* h(\theta)\}\right)^2}. \tag{24}$$

When the beam pattern phase is constant with respect to θ, that is, $\operatorname{Im}\{h'(\theta)^* h(\theta)\} = 0$. Equation (24) can be reduced to the simpler form

$$\operatorname{Var}\left\{\hat{\theta}\right\} \geq \frac{\sigma^2}{2M|\alpha|^2 |h'(\theta)|^2}. \tag{25}$$

Taking the square root gives the RMSE form

$$\sqrt{\operatorname{CRLB}(\theta)} = \sqrt{\frac{\sigma^2}{2M|\alpha|^2 |h'(\theta)|^2}}. \tag{26}$$

Finally, by inserting the explicit form of the beam-pattern gain $h(\theta)$ and its derivative $h'(\theta)$ given by our closed-form path loss expressions in (8) and (16), we obtain a completely analytical curve $(\operatorname{CRLB}(\theta))^{1/2}$ that depends only on known system parameters, the measurement noise variance σ^2, and the number of snapshots M. The result of comparing CRLB to the actual RMSE of the estimation is shown in Fig. 11. We assume the noise variance $\sigma^2 = 10^{-3}$ and the number of snapshots

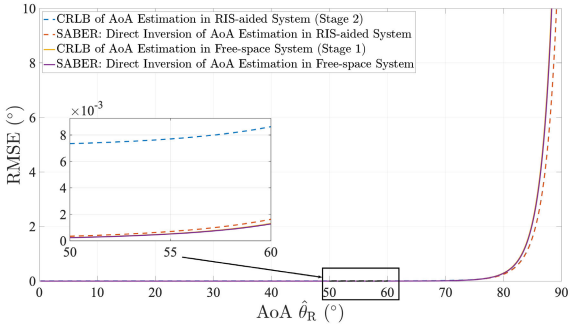

Fig. 11. Empirical RMSE of SABER: direct inversion compared with the CRLBs of each stage, where free-space is shown in solid lines, while the RIS-aided case is shown in dashed lines.

M equal to 1000. The results of the free-space (Stage I) and RIS-aided system (Stage II) are shown in solid and dashed lines, respectively. Moreover, the inset highlights the region between $\hat{\theta}_R = 50°$ and $\hat{\theta}_R = 60°$, where the difference between the CRLB and the achieved RMSE is on the order of 10^{-3} degrees. In particular, SABER: direct inversion in Stage I is almost indistinguishable from the CRLB curve, while in Stage II, a slight but consistent gap remains, with SABER (red dashed line) following the same trend as the RIS-aided CRLB but at a marginally higher RMSE level. This close agreement demonstrates that SABER operates near the fundamental estimation limit for both tested configurations, confirming their statistical efficiency and robustness even under different propagation conditions. As expected from the derivative term in the CRLB expression, the bound sharply increases as θ approaches 90°, reflecting the loss of angular sensitivity when the array is illuminated from the direction that is parallel to the radiation pattern of the received terminal. This behavior is not solely a theoretical phenomenon; from a hardware perspective, handling large-angle oblique incidence remains a significant challenge. Even in advanced beam-steering systems, achieving reliable performance at extreme steering angles is difficult, highlighting the practical relevance of the divergence near 90° [49], which can cause beam alignment to be ill-conditioned and increase the risk of mispointing.

D. Computational Complexity

Finally, we analyze the computational complexity and energy cost of the three proposed SR-based approaches. In addition, we adopt the energy calculation in [50], where the simulation is run on an Apple M1 Pro central processing unit (CPU) with maximum power of 30 W. As illustrated in Fig. 12, since all approaches utilize an identical hyperparameter configuration (e.g., number of iterations and population size), their theoretical search space complexity remains consistent in terms of Floating-point operations per cycle per core (FLOPs) (1.36×10^{11} FLOPs). However, significant differences emerge in their empirical training durations and energy consumption. Particularly, the unconstrained-SR approach exhibits the highest computational overhead, necessitating approximately 26 s for training and consuming 782 J of energy. Meanwhile, the SABER direct inversion method offers an intermediate performance, reducing training time to 16.4 s and energy to 493 J by constraining the search space with domain knowledge.

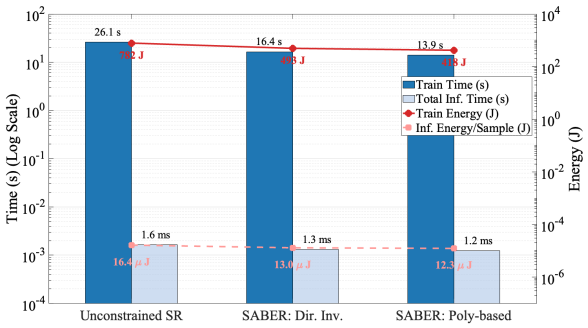

Fig. 12. Computational complexity and energy consumption analysis of the proposed SR-based methods. The left axis (bar chart) displays the training and inference time on a logarithmic scale, while the right axis (line plot) illustrates the corresponding energy consumption. All methods share identical hyperparameter configurations, highlighting the efficiency gains of the constrained SABER approaches.

On the other hand, the SABER polynomial-based cosine inversion proves to be the most efficient, further reducing the training time to 13.9 s and energy consumption to 418 J, a reduction directly attributable to its simplified operator search space and avoidance of expensive transcendental operations. Crucial for real-time applications, the closed-form estimators offer $O(1)$ constant-time inference with negligible latency (milliseconds) and energy cost (micro Joules) per sample. This offers a distinct advantage over lightweight iterative numerical inversions, whose complexity scales with the required number of iterations to achieve convergence.

The inference latency and energy cost per sample for all methods are negligible (on the order of milliseconds and micro Joules, respectively). However, this efficiency introduces a design tradeoff between accuracy and cost. While the polynomial-based cosine inversion approach minimizes computational complexity and therefore energy usage, it inherently approximates the analytical inverse, yielding higher estimation errors compared to the physically exact direct inversion. Consequently, the optimal choice depends on the specific deployment scenario. For example, SABER: direct inversion is preferable for high- precision applications, such as mmWave beam alignment, whereas the polynomial-based variant is ideal for latency-critical IHRLLC, as well as providing services on ultralow- power edge devices, thereby confirming the versatility of SABER across diverse 6G ecosystems.

VIII. Conclusion and Future Work

In this work, we introduced SABER, an SR-based solution for AoA estimation that relies solely on the measured path loss coefficient. Specifically, we employed an SR-based ML framework to recover antenna directivity and beam pattern characteristics, enabling interpretable AoA estimation in both a controlled free-space setup and a realistic RIS-aided indoor testbed. Unlike many ML-based methods, SABER achieves not only high accuracy but also interpretable closed-form models, facilitating future integration into physics-aware design and analysis. More specifically, in Stage I, covering a multiangle sweep in free space, we showed that embedding minimal prior knowledge: either the exact $\cos^n$ form or a low-order polynomial surrogate, as well as the relationship between path loss coefficient and the AoA. We can preserve near-optimal performance (MAE = 0.42°), while guaranteeing physical transparency and consistent extrapolation. In contrast, unconstrained SR achieved the lowest prediction error (MAE = 0.396°) but produced highly complex, nonintuitive expressions.

On the other hand, in Stage II, where the AoA was fixed and deterministic in a RIS-aided setup, the unconstrained SR approach achieved both high accuracy (MAE = 6.53×10^{-7}) and interpretability, indicating that prior beam pattern knowledge is not strictly necessary in such single-angle estimation tasks. These findings demonstrate that unconstrained SR maintains high accuracy across both scenarios, but its interpretability depends on the nature of the estimation problem: prior knowledge is valuable for multiangle estimation, whereas simpler, fixed-angle cases can achieve a natural balance between accuracy and interpretability without it. Moreover, by benchmarking against the theoretical CRLB bounds, SABER showed near-optimal performance. Furthermore, the experimental validation in the RIS-aided indoor environment demonstrates the robustness of SABER to signal interference. By deriving the scattering parameter S_{21} in a rms sense and employing temporal averaging consistent with the channel coherence time, the impact of multipath propagation is effectively mitigated, confirming the method's applicability in less ideal propagation scenarios.

While the proposed SABER framework demonstrates high accuracy in single-source scenarios and robustness to static multipath via rms averaging, we acknowledge the challenges posed by highly dynamic and multiuser environments. Specifically, relying on a scalar path loss coefficient limits the ability to distinguish multiple simultaneous AoA or concurrent users, and inherently restricts the unambiguous estimation range if the antenna exhibits high sidelobe levels. Therefore, the current approach is best suited for scenarios where a single dominant LoS path exists. To address this, future investigations will extend the analysis to multibeam conditions and scenarios with higher sidelobe levels, assessing the boundaries of the current cosine-based approximation. Furthermore, to extend the applicability of SABER to mobile and multiuser scenarios, we will explore expanding the input feature space by incorporating vector inputs, such as multifrequency magnitude snapshots or temporal sequences, to resolve multiple simultaneous signal sources. As part of these future experimental studies, we intend to rigorously evaluate the system's robustness by testing its estimation capabilities in the presence of interfering signals with power levels similar to the main source. In addition, we plan to investigate adaptive averaging windows that can accommodate the coherence time of mobile users, thereby addressing the temporal dynamics of nonstationary channels.

References

[1] P. Popovski et al., "Wireless access in ultra-reliable low-latency communication (URLLC)," *IEEE Trans. Commun.*, vol. 67, no. 8, pp. 5783–5801, Aug. 2019.

[2] A. A. Shamsabadi, A. Yadav, Y. Gadallah, and H. Yanikomeroglu, "Exploring the 6G potentials: Immersive, hyper reliable, and low-latency communication," 2025, *arXiv:2407.11051*.

[3] X. Di et al., "AI-powered urban transportation digital twin: Methods and applications," 2024, *arXiv:2501.10396*.

[4] T. S. Rappaport et al., "Millimeter wave mobile communications for 5G cellular: It will work!," *IEEE Access*, vol. 1, pp. 335–349, 2013.

[5] H. Sarieddeen, M.-S. Alouini, and T. Y. Al-Naffouri, "Terahertz-band ultra-massive spatial modulation MIMO," *IEEE J. Sel. Areas Commun.*, vol. 37, no. 9, pp. 2040–2052, Sep. 2019.

[6] H. Q. Ngo, G. Interdonato, E. G. Larsson, G. Caire, and J. G. Andrews, "Ultra-dense cell-free massive MIMO for 6G: Technical overview and open questions," 2024, *arXiv:2401.03898*.

[7] C. Jiang, C. Zhang, C. Huang, J. Ge, D. Niyato, and C. Yuen, "RIS-assisted ISAC systems for robust secure transmission with imperfect sense estimation," *IEEE Trans. Wireless Commun.*, vol. 24, no. 5, pp. 3979–3992, May 2025.

[8] M. A. G. Al-Sadoon, R. Asif, Y. I. A. Al-Yasir, R. A. Abd-Alhameed, and P. S. Excell, "AOA localization for vehicle-tracking systems using a dual-band sensor array," *IEEE Trans. Antennas Propag.*, vol. 68, no. 8, pp. 6330–6345, Aug. 2020.

[9] Rustamaji, S. Kliwati, and W. Widada, "The angle of arrival estimation of frequency-hopping cooperative object based on software-defined radio," *Sci. Rep.*, vol. 14, no. 1, p. 7732, Apr. 2024, doi: 10.1038/s41598-024-58488-8.

[10] M. E. Morocho-Cayamcela, H. Lee, and W. Lim, "Machine learning for 5G/B5G mobile and wireless communications: Potential, limitations, and future directions," *IEEE Access*, vol. 7, pp. 137184–137206, 2019.

[11] R. Schmidt, "Multiple emitter location and signal parameter estimation," *IEEE Trans. Antennas Propag.*, vol. AP-34, no. 3, pp. 276–280, Mar. 1986.

[12] R. Roy and T. Kailath, "ESPRIT-estimation of signal parameters via rotational invariance techniques," *IEEE Trans. Acoust., Speech, Signal Process.*, vol. 37, no. 7, pp. 984–995, Jul. 1989.

[13] W. Li, Z. Zhu, W. Gao, and W. Liao, "Stability and super-resolution of MUSIC and ESPRIT for multi-snapshot spectral estimation," *IEEE Trans. Signal Process.*, vol. 70, pp. 4555–4570, 2022.

[14] H. Ramoser, J. Müller-Gerking, and G. Pfurtscheller, "Optimal spatial filtering of single trial EEG during imagined hand movement," *IEEE Trans. Rehabil. Eng.*, vol. 8, no. 4, pp. 441–446, Dec. 2000.

[15] X. Yang, R. Tong, M. Zhou, J. Wang, T. Zhang, and J. Cheng, "Indoor localization using low-rank matrix recovery and dynamic parameter estimation algorithm with commodity Wi-Fi," *IEEE Trans. Instrum. Meas.*, vol. 74, pp. 1–17, 2025.

[16] Y. Yuan, L. Zhou, S. Wang, Y. Guo, K. Ma, and Z. Liu, "High-precision 3-D indoor localization using pseudo-centroid AoA estimation and adaptive channel preference with URAs," *IEEE Trans. Instrum. Meas.*, vol. 74, pp. 1–10, 2025.

[17] A. Xhafa, F. Fabra, D. Egea-Roca, J. A. López-Salcedo, and G. Seco-Granados, "Experimental investigation of AoA estimation and antenna calibration with 5G NR SignalsUsing USRP devices," *IEEE Trans. Instrum. Meas.*, vol. 74, pp. 1–15, 2025.

[18] T. Margiani, S. Cortesi, M. Keller, C. Vogt, T. Polonelli, and M. Magno, "Angle of arrival and centimeter distance estimation on a smart UWB sensor node," *IEEE Trans. Instrum. Meas.*, vol. 72, pp. 1–10, 2023.

[19] B. W. Domae, R. Li, and D. Cabric, "Machine learning assisted phaseless millimeter-wave beam alignment in multipath channels," in *Proc. IEEE Global Commun. Conf. (GLOBECOM)*, Dec. 2021, pp. 1–7.

[20] H. Hassanieh, O. Abari, M. Rodriguez, M. Abdelghany, D. Katabi, and P. Indyk, "Fast millimeter wave beam alignment," in *Proc. Conf. ACM Special Interest Group Data Commun.*, Aug. 2018, pp. 432–445, doi: 10.1145/3230543.3230581.

[21] J. Zhang, G. Zheng, Y. Zhang, I. Krikidis, and K.-K. Wong, "Deep learning based predictive beamforming design," *IEEE Trans. Veh. Technol.*, vol. 72, no. 6, pp. 8122–8127, Jun. 2023.

[22] N. Jayaweera et al., "5G-advanced AI/ML beam management: Performance evaluation with integrated ML models," 2024, *arXiv:2404.15326*.

[23] Q. Xue, A. Nordio, K. Niu, C. Dong, and C. Fabiana Chiasserini, "Integrated probing-beam pattern learning and beam prediction for mmWave massive MIMO," *IEEE Trans. Commun.*, vol. 73, no. 8, pp. 6499–6513, Aug. 2025.

[24] S. Ge, K. Li, and S. N. B. M. Rum, "Deep learning approach in DOA estimation: A systematic literature review," *Mobile Inf. Syst.*, vol. 2021, pp. 1–14, Sep. 2021, doi: 10.1155/2021/6392875.

[25] A. Khan, S. Wang, and Z. Zhu, "Angle-of-arrival estimation using an adaptive machine learning framework," *IEEE Commun. Lett.*, vol. 23, no. 2, pp. 294–297, Feb. 2019.

[26] G. K. Papageorgiou, M. Sellathurai, and Y. C. Eldar, "Deep networks for direction-of-arrival estimation in low SNR," *IEEE Trans. Signal Process.*, vol. 69, pp. 3714–3729, 2021.

[27] C. M. Mylonakis, P. Velanas, P. I. Lazaridis, P. Sarigiannidis, S. K. Goudos, and Z. D. Zaharis, "3D direction of arrival estimation: An innovative deep neural network approach," in *Proc. 13th Int. Conf. Mod. Circuits Syst. Technol. (MOCAST)*, 2024, pp. 01–04.

[28] W. Wu, D. Zhou, L. Shen, Z. Zhao, C. Li, and G. Q. Huang, "TransAoA: Transformer-based angle of arrival estimation for BLE indoor localization," *IEEE Trans. Instrum. Meas.*, vol. 74, pp. 1–12, 2025.

[29] X. Niu, X. Su, L. He, and G. Chen, "Direction of arrival (DOA) estimation using a deep unfolded learned iterative shrinkage thresholding algorithm (LISTA) network in a non-uniform metasurface," *Remote Sens.*, vol. 17, no. 7, p. 1253, Apr. 2025. [Online]. Available: https://www.mdpi.com/2072-4292/17/7/1253

[30] Y. Azhdari and M. Farhang, "Neural network-based intelligent reflecting surface assisted direction of arrival estimation," 2025, *arXiv:2406.18306*.

[31] D. T. Phan, Q. D. Nguyen, N. Takanen, T. N. Nguyen, M. Juntti, and P. J. Soh, "ML-assisted RIS for ISAC systems: Initial results in the 6G study band," in *Proc. 19th Eur. Conf. Antennas Propag. (EuCAP)*, Mar. 2025, pp. 1–5.

[32] D. Lloria, S. Roger, C. Botella-Mascarell, and M. Cobos, "Deep learning based AoA and AoD estimation for millimeter wave MIMO systems," in *Proc. 12th Euro Amer. Conf. Telematics Inf. Syst.*, Jul. 2024, pp. 1–4, doi: 10.1145/3685243.3685247.

[33] T. C. Rapudu and O. O. Oyerinde, "Machine learning-based channel estimation for multi-RIS-assisted mmWave massive-MIMO OFDM system in a dynamic environment," *IEEE Trans. Wireless Commun.*, vol. 24, no. 6, pp. 5297–5309, Jun. 2025.

[34] N. Deng and M. Haenggi, "A novel approximate antenna pattern for directional antenna arrays," *IEEE Wireless Commun. Lett.*, vol. 7, no. 5, pp. 832–835, Oct. 2018.

[35] S.-K. Chou, O. Yurduseven, H. Q. Ngo, and M. Matthaiou, "On the aperture efficiency of intelligent reflecting surfaces," *IEEE Wireless Commun. Lett.*, vol. 10, no. 3, pp. 599–603, Mar. 2021.

[36] A. Anaqreh, S.-K. Chou, M. Mohorcic, T. Lagkas, and C. Fortuna, "Automated modeling method for pathloss model discovery," 2025, *arXiv:2505.23383*.

[37] C. F. Hayes et al., "Deep symbolic optimization: Reinforcement learning for symbolic mathematics," 2025, *arXiv:2505.10762*.

[38] T. N. Mundhenk et al., "Symbolic regression via neural-guided genetic programming population seeding," 2021, *arXiv:2111.00053*.

[39] M. J. Kusner, B. Paige, and J. M. Hernández-Lobato, "Grammar variational autoencoder," 2017, *arXiv:1703.01925*.

[40] S.-M. Udrescu and M. Tegmark, "AI Feynman: A physics-inspired method for symbolic regression," 2020, *arXiv:1905.11481*.

[41] (2020). *R&S ZVA / ZVB / ZVT Vector Network Analyzers Operating Manual*. [Online]. Available: https://scdn.rohde-schwarz.com/ur/pws/dl_downloads/dl_common_library/dl_manuals/dl_user_manual/ZVA_ZVB_ZVT_OperatingManual_en_33.pdf

[42] C.-N. Hu, Y.-X. Li, and K.-C. Chou, "Research on millimeter-wave phased antenna array for wireless communication applications," in *Proc. IEEE 12th Asia–Pacific Conf. Antennas Propag. (APCAP)*, Sep. 2024, pp. 1–2.

[43] C.-N. Hu et al., "Passive reconfigurable intelligent surface (RIS) for enhanced wireless communications," in *Proc. Photon. Electromagn. Res. Symp. (PIERS)*, Apr. 2024, pp. 1–4.

[44] (2020). *F6522 Short-Form Datasheet: 8-Ch Tx Active Beamforming IC 27.5–31.0 GHz*. [Online]. Available: https://www.renesas.com/en/document/sds/f6522-short-form-datasheet

[45] M. Cranmer, "Interpretable machine learning for science with PySR and symbolic regression," 2023, *arXiv:2305.01582*.

[46] Z. Dai, Y. He, V. Tran, N. Trigoni, and A. Markham, "DeepAoANet: Learning angle of arrival from software defined radios with deep neural networks," *IEEE Access*, vol. 10, pp. 3164–3176, 2022.

[47] H. L. V. Trees, *Detection, Estimation, and Modulation Theory*. Hoboken, NJ, USA: Wiley, 2001.

[48] H. Steendam, T. Q. Wang, and J. Armstrong, "Cramer–Rao bound for AOA-based VLP with an aperture-based receiver," in *Proc. IEEE Int. Conf. Commun. (ICC)*, May 2017, pp. 1–6.

[49] G. Xie et al., "Demonstration of tunable steering and multiplexing of two 28 GHz data carrying orbital angular momentum beams using antenna array," *Sci. Rep.*, vol. 6, no. 1, p. 37078, Nov. 2016.

[50] S.-K. Chou, J. Hribar, V. Hanžel, M. Mohorčić, and C. Fortuna, "The energy cost of artificial intelligence lifecycle in communication networks," *IEEE J. Sel. Areas Commun.*, vol. 44, pp. 2427–2443, 2026.